Numerical Methods in Civil Engineering, 8-1 (2023) 01-17

Numerical Methods in Civil Engineering

Journal Homepage: https://nmce.kntu.ac.ir/

SPH Technique to Study the Sloshing in Concrete Liquid Tanks

Seyyed Mesiam Aghajanzadeh [*], Hasan Mirzabozorg [**], and Homayoon Yazdani [***]

ARTICLE INFO

RESEARCH PAPER

Article history:
Received:
April 2023.
Revised:
July 2023.
Accepted:
July 2023.

Keywords:
FE-SPH coupling,
Hydrodynamic pressure,
Roofed tanks,
Sloshing,
Taguchi method

Abstract:

This study aims to consider the sloshing height and hydrodynamic pressure in roofless and roofed liquid storage tanks utilizing a coupled FE-SPH technique. As a design technique for determining the necessary analyses and main parameters to reach reasonable results, the Taguchi method is used. The SPH formulation models the liquid concerning the large amplitude sloshing waves, and the finite element method simulates the structure. At first, it is found that expressions presented in ACI 350.3-06 should be revised when calculating the sloshing height in a rectangular tank. Secondly, when determining the hydrodynamic pressure applied on the roof and, also the sloshing height, the frequency content of the input ground motion affects significantly the contained liquid responses. Comparison of the results obtained for roofed and roofless tanks indicate no clear correlation between their dynamic responses. The results of this study suggest the ratio of liquid height to its length, the length itself, and earthquake record PGA as noise parameters in Taguchi analysis. At last, the suggested Taguchi analysis's main design parameters for future studies are the acceleration spectrum intensity ASI and the liquid's height in the storage tank.

1. Introduction

As an essential part of the contemporary built environment, liquid storage tanks are widespread that serve various purposes. In these structures, the liquid-free surface motion during an earthquake applies considerable loads to their walls and roof. This seismic response, which is named sloshing, is in the category of fluid-structure interaction problems. Many challenging issues exist in this field of engineering despite the wide range of studies conducted on the sloshing wave's effects on liquid storage tanks.

Up to now, various approaches have been proposed to formulate the sloshing in storage tanks. Someone categorizes the introduced approaches as the analytical solutions; experimental methods; and numerical techniques. Analytical solutions of the sloshing phenomenon as a fluid-structure interaction problem, including the partial differential equations of field problems, are troublesome.

Westergaard in 1933 investigated the hydrodynamic pressure in a rigid dam having a rectangular medium in its upstream as the reservoir, which led to some analytical expressions [1]. Later, for the first time, Jacobsen in 1949 studied seismic responses of partially filled tanks under a horizontal ground displacement [2]. Housner in 1957 introduced the first practical, simplified formulas for calculating the fluid container's sloshing forces [3]. He proposed approximate solutions in simple forms instead of solving partial differential equations and infinite series associated with Laplace's equation. He introduced the impulsive and convective pressures and investigated these two components of pressures, separately. He mentioned that convective pressures are the consequences of impulsive pressures. Based on this categorization, the sloshing waves are due to convective pressure. Later, in another study, Housner in 1963 recommended some simple formulas to take into account for the water and tank's relative motions

* *PhD in Structural Engineering, Civil Engineering Department, K. N. Toosi University of Technology, Tehran, Iran.*
** *Corresponding Author: Associate Professor, Civil Engineering Department, K. N. Toosi University of Technology, Tehran, Iran. Email: mirzabozorg@kntu.ac.ir*
*** *Graduate Student in Structural Engineering, Civil Engineering Department, K. N. Toosi University of Technology, Tehran, Iran.*

https://doi.org/10.61186/NMCE.2304.1015

investigating the damaged liquid container during the Chilean earthquake [4].

Apart from these preliminary analytical solutions, by computer development, proposing more sophisticated numerical methods, and more advanced and accurate laboratory equipment, more detailed complex analyses have been conducted in fluid-structures interaction problems [5-7]. Babu and Bhattacharyya established a numerical model using the finite element approach to determine the sloshing height and the associated pressure applied on the liquid tanks' wall [9]. Virella et al. studied the nonlinear wave theory effects on the sloshing phenomena responses by the finite element method [10]. Kianoush and Ghaemmaghami developed a three-dimensional finite element model of partially filled concrete rectangular tanks to analyze the earthquake frequency content effects on sloshing wave characteristics [11]. Manser et al. modeled three-dimensional cylindrical reservoirs with a metal shell containing liquid employing the finite element method [12]. Zhang and Wang used the fully Lagrangian particle method combined with the finite element method to investigate sloshing loads' impact numerically [13].

Despite the wide application of the finite element method, this technique, as a grid-based numerical method, has some deficiency for modeling the sloshing phenomenon because of sloshing large amplitude motion, which causes the high geometric distortion in elements. Solving the shortages, a more compatible meshless numerical method with hydrodynamic issues, called Smoothed Particle Method, is employed. This approach is a particle-based mesh-free Lagrangian method popular in hydrodynamic problems because of its formulations, including mass and density [14]. Unlike the conventional grid-based methods, this method is an appropriate solution for large deformation problems such as sloshing wave which employs the moving particles. After the initial development of the Smoothed Particle Method SPH by Gingold and Monaghan [15] and Lucy [16] in 1977 for simulating astrophysics problems, this method was widely adapted to different engineering problems.

Recently, SPH formulations have received much attention to solving fluid-structure interaction problems. Groenenboom et al. studied the coupled FE-SPH technique's accuracy to solve the fluid-structure interaction problem [17]. Hu et al. introduced Striped-Point-In-Box S-PIB to modify neighbor searching and contact searching deficiencies when the SPH approach is coupled with the finite element method in fluid-structure interaction problems [18]. Ramirez et al. solved nonlinear transient fluid-structure interaction, including coupled FE-SPH [19]. They adopted different incompatible time steps in their solution. Han and Hu solved the artificial strain and stress problems under a rigid coordinate transformation which can be applied to the structures by suggesting a numerical simulation of FSI problems based on the SPH formulations [20]. Jena and Biswal employed the moving particle semi-implicit MPS method as a mesh-free particle approach to simulate the sloshing phenomena. They concluded mesh particle-free method could successfully model the dynamic parameters of partially filled liquid containers [21]. Xu et al. showed that a coupled numerical manifold method approach NMM-SPH, including their proposed contact algorithm, predicts the discontinuous deformation and stress field of fluid-structure interaction [22]. Dincer et al. investigated fluid interaction with a free surface in contact with an elastic structure using the coupled FE-SPH [23]. Moslemi et al. investigated the nonlinear sloshing phenomenon in rectangular liquid storage tanks by FE-SPH coupled method [24]. Ng et al. investigated the fluid-structure interaction problem introducing a unified particle model that couples the SPH and the volume compensated particle method [25]. Kalateh and Koosheh modeled the cavitating fluid interaction with the convergent-divergent nozzle, improving the SPH approach's combination with the finite element method to solve the multiphase fluid-structure interaction problem [26].

The current practice includes the coupled FE-SPH technique to study the sloshing phenomenon including the sloshing height in roofless tanks and the upward hydrodynamic pressure applied on the roof in roofed tanks in two-dimensional rectangular tanks under seismic excitation. Moslemi et al. investigated the phenomenon of sloshing using the coupled FE-SPH technique for roofless tanks [24]. In this study, using the coupled FE-SPH technique, in addition to roofless tanks, the dynamic responses of roofed tanks are also investigated. After validating the numerical model, horizontal components of three scaled earthquake records covering the low to high frequencies are applied to the provided models of tanks which their geometric dimensions are set using the Taguchi method, where the liquid height and the ratio of the height to its length are the main geometric parameters. Next, a comprehensive interpretation of results is presented in which the role of each examined parameter in the sloshing phenomenon is considered. At last, some practical suggestions are presented concerning the ACI 350.3-06 and the Taguchi method parameters.

2. SPH Method

The SPH solution consists of two main steps: 1-representing the field function by its equivalent representation and 2-discretizing the integral approximation by a finite number of particles (particle approximation). The particle approximation includes the particles within the support domain. These associated particles have the individual mass that occupies a particular space. Based on these two steps, the field function f(x) is approximated as follows:

$$f(x) = \sum_{j=1}^{N} \frac{m_j}{\rho_j} W\left(X - X_j, h\right) f\left(X_j\right) \quad (1)$$

where, m_j is the mass of particle j, ρ_j is the density of particle j, W is the smoothing function, N is the number of particles within the support domain of particle j, and X is the three-dimensional position vector. The SPH method replaces the delta function Kernel δ by a smoothing Kernel function to solve the integral representation numerically.

1.1 SPH Formulation of Navier-Stokes Equations

Navier-Stokes equations govern the incompressible, viscous, and homogenous fluid motion, which considers conservation of mass, momentum, and energy, including the following equations:

1- The continuity equation:

$$\frac{D\rho}{Dt} = -\rho \frac{\partial v^{\beta}}{\partial x^{\beta}} \quad (2)$$

2- The momentum equation:

$$\frac{Dv^{\alpha}}{Dt} = \frac{1}{t} \frac{\partial \sigma^{\alpha\beta}}{\partial x^{\beta}} \quad (3)$$

3- The energy equation:

$$\frac{De}{Dt} = \frac{\sigma^{\alpha\beta}}{\rho} \frac{\partial v^{\alpha}}{\partial x^{\beta}} \quad (4)$$

where α and β show the coordinate directions, σ is the total stress tensor including isotropic pressure and viscous stress, ρ is density, ν is vector velocity, and x is the position vector. Liu and Liu developed the modified SPH method to introduce artificial viscosity and artificial heat into the SPH formulation [14]. The SPH formulation of Navier-Stokes equations considering modification proposed by Liu and Liu are defined by:

$$\frac{D\rho_i}{Dt} = \sum_{j=1}^{N} m_j v_{ij}^{\beta} \frac{\partial W_{ij}}{\partial x_i^{\beta}} \quad (5)$$

$$\frac{Dv_i^{\alpha}}{Dt} = -\sum_{j=1}^{n} m_j \left(\frac{\sigma_i^{\alpha\beta}}{\rho_i^2} + \frac{\sigma_j^{\alpha\beta}}{\rho_j^2} + \Pi_{ij} \right) \frac{\partial W_{ij}}{\partial x_i^{\beta}} \quad (6)$$

$$\frac{De_i}{Dt} = \frac{1}{2} \sum_{j=1}^{N} m_j \left(\frac{p_i}{\rho_i^2} + \frac{p_j}{\rho_j^2} + \Pi_{ij} \right) v_{ij}^{\beta} + \frac{\mu_i}{2\rho_i} \varepsilon_i^{\alpha\beta} \varepsilon_i^{\alpha\beta} + H_i \quad (7)$$

$$\frac{Dx_i^{\alpha}}{Dt} = v_i^{\alpha} \quad (8)$$

where ν, e, t, and x are the velocity, energy, time, and coordinates. Π_{ij} and H_i denote the artificial viscosity and heat, respectively. W_{ij} is the smoothed function of a pair of particles i and j. μ_i is the dynamic viscosity of particle i, and ε_i is the viscous shear stress of particle i.

1.2 Constitutive Model

The liquid material used for this study is water, in which the following viscous constitutive equation models the liquid motion [27]:

$$\sigma_{ij} = 2v_d \dot{\varepsilon}'_{ij} - P\delta_{ij} \quad (9)$$

where, υ_d is the dynamic viscosity, is the deviatoric strain rate, and δ_{ij} is the identity tensor.

Further, the Gruneisen equation of state (EOS) calculates the pressure P of water as follows:

1-For compressed state (μ>0):

$$P = \frac{\rho_0 C^2 \mu \left[1 + \left(1 - \frac{\gamma_0}{2}\right)\mu - \frac{a}{2}\mu^2\right]}{\left[1 - (S_1 - 1)\mu - S_2 \frac{\mu^2}{\mu+1} - S_3 \frac{\mu^3}{(\mu+1)^2}\right]} + (\gamma_0 + a\mu)E \quad (10)$$

2-For Expansion state:

$$P = \rho_0 D^2 \mu + (\gamma_0 + a\mu)E \quad (11)$$

where, $\mu = \frac{\rho}{\rho_0} - 1$ and ρ and ρ_0 are the current and initial densities of the material, respectively. E represents the internal energy of the fluid per initial volume. C, S_1, S_2, S_3, γ_0, and a are EOS coefficients.

3. Taguchi Method

Taguchi method is an approach that advises some techniques for planning parameter design experiments to determine the best combination of design variables that reduce the influences of the design process to the source of variation instead of controlling these sources [28-31]. As an off-line quality control method, Parameter design divides the variable into two categories of design parameters and source of noises. Kachar mentioned that the noise sources are the reason for the performance variations (functional variation) [28].

Taguchi method evaluates the effect of noise factors employing a signal to noise ratio to compare multiple (different) settings of parameters to minimize the loss function. Among over 60 signal-to-noise ratios proposed by the Taguchi method, the three most popular signal-to-noise ratios of the Taguchi method are 1- "the smaller is the better", 2- "the larger is the better", and 3- "a specific target value is best" [30]. This study employs "the smaller is the better" as the signal-to-noise ratio. The expression for "the smaller is the better" is the following formulation

$$\frac{S}{N} = -10 \times \log\left(\frac{\sum y_i^2}{n}\right) \quad (12)$$

where S/N is the signal-to-noise ratio, n is the number of noise matrix rows.

4. Numerical Studies

This section deals with the influences of geometric dimensions and frequency contents on the sloshing phenomena, including the provided numerical FE-SPH coupled models. The tank is fixed at the base, and the effects of base uplift and soil flexibility are ignored. The liquid domain is modeled as particles. Figure 1 shows a schematic view of tank geometric parameters. H_l, H_w, and L_x are the height of the liquid, the height of the tank, and half of the tank length, respectively. Sidewalls thickness t_w is 500mm. Seismic loads are applied in the horizontal direction, and the maximum sloshing responses are calculated at Point A.

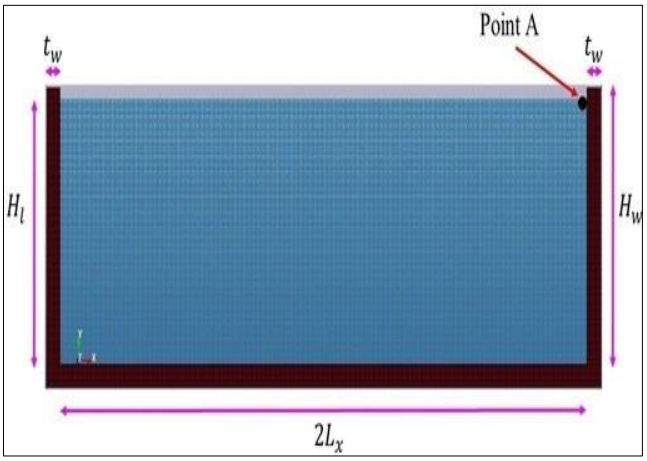

Fig. 1: Two-dimensional model of a partially filled rectangular tank

This study considers three levels of $\frac{H_l}{2L_x}$, three levels of H_l, and three earthquake excitations. Accordingly, it is necessary to consider 3×3×3 different analyses in which H_l and $\frac{H_l}{2L_x}$ have a specific value under each earthquake excitation. Instead of performing 27 separate analyzes, only nine models with different geometric properties are considered based on the Taguchi method idea and optimization of analyzes so that the geometric parameters values and the earthquake records selection for each analysis are determined using the Taguchi method to increase analysis eficiency. In this regard, these nine models are divided into three separate subgroups. Each subgroup, consisting of three tanks with different geometric characteristics, is subjected to an individual earthquake record. The provided FE-SPH models contain both roofed and roofless tanks. Sloshing height is calculated for the roofless tanks, and hydrodynamic pressure applied on the roof is obtained for the roofed tanks. The signal to noise ratios are calculated based on the "smaller is the better".

4.1 Seismic Loading

The horizontal components of Northridge (1994), El-Centro (1940), and Landers (1992) earthquakes are applied to the liquid storage tanks. The components are scaled so that the peak ground acceleration reaches 0.4g. Analyses are performed for the first 20s of each excitation, with time intervals of 0.005s. Figures 2(a) to 2(c) show the original earthquake components of Northridge (1994), El-Centro (1940), and Landers (1992) [32].

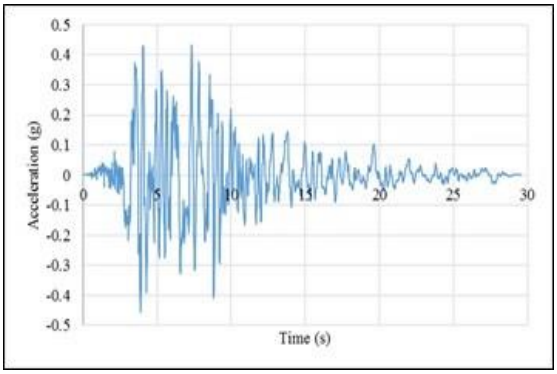

(a)

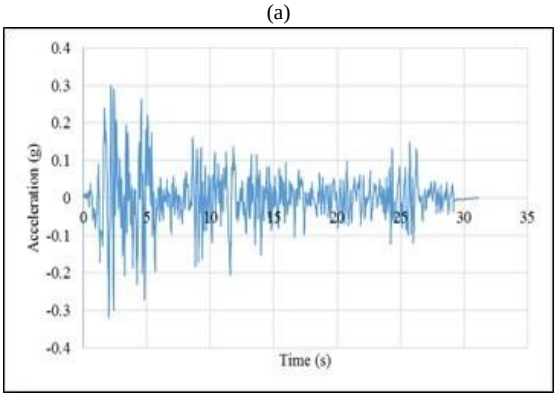

(b)

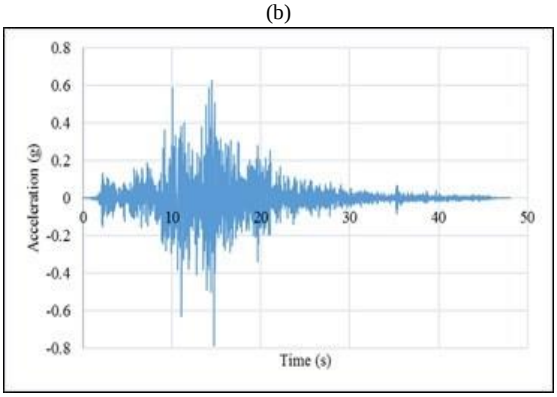

(c)

Fig. 2: Earthquake records used as seismic loading [32]

Additionally, this study considers the ratio of peak ground acceleration (PGA), which is expressed in units of g, to peak ground velocity (PGV), expressed in units of (m/s) to investigate the earthquake frequency content effects on sloshing wave properties [33]. Table 1 shows these earthquake components' properties.

Table 1: Seismic excitations characteristics

Name	Year	Magnitude	Rjb (Km)	PGA (g)	PGV (m/s)	PGA/PGV (1/s)
Northridge	1994	6.69	0	0.457	0.7484	0.61
El-Centro	1940	6.95	6.09	0.319	0.3614	0.88
Landers	1992	7.28	2.19	0.782	0.3241	2.41

4.2 Verification Analysis

The provided numerical model is verified with the study conducted by Kianoush et al. [34]. They carried out numerical analyses using the finite element method for a 2D partially filled liquid-tank system. In their study, H_l, H_w, $2L_x$ and t_w are 6m, 6.5m, 20m and 500mm, respectively, and the elastic modulus E_c, the density ρ_c and the Poison's ratio ν for the concrete lateral walls are 26.64 GPa, 2400 kg/m^3 and 0.17, respectively.

In the current study, for verification analyses the liquid inside the storage tanks is simulated using two different techniques: the finite element method, and the smoothed particles modeling. Responses resulted from both techniques are compared with those reported by Kianoush et al. [34]. Table 2 summarizes the constants' values for Gruneisen equation of state EOS used in SPH modeling in the liquid domain.

Table 2: Material and EOS parameters used in the liquid domain [27]

Parameter	ρ_0	ν_d	C	S_1	S_2	S_3	γ_0	a	E_0	V_0
Value	1000 kg/m^3	0.001 Pa.s	1448 m/s	1.979	0	0	0.11	3	0 J	0 m/s

In this table, ρ_0, ν_d, C, and V0 are the initial density, the dynamic viscosity, the speed of sound in liquid, and the initial relative volume of liquid. Also, S_1, S_2, S_3, γ_0, and a are EOS coeficients. El-Centro 1940 earthquake record shown in Figure 2(b) is selected as the external base excitation. The component is scaled so that the peak ground acceleration reaches 0.4g. Figure 3 and Table 3 compare the maximum sloshing height.

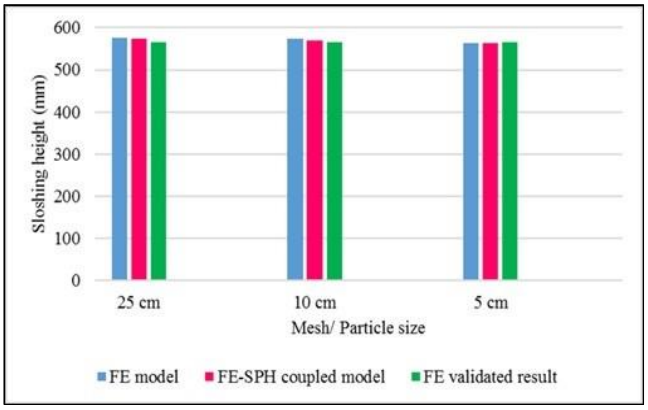

Fig. 3: Comparison of the FE model, the FE-SPH coupled and Kianoush et al. [34]

Table 3: Sloshing height-FE method and FE-SPH coupled approach compared with Kianoush et al. [34]

Part	mesh size (cm)		FE	FE-SPH		Validation	Difference (%)	
	Horizontal	Vertical	Elements	Elements	Particles	Elements	FE	FE-SPH
fluid	25	25	576	574	1920	565	1.9	1.6
wall	25	25						
fluid	10	10	573	569	12000	565	1.4	0.7
wall	10	10						
fluid	5	5	564	563	48000	565	0.2	0.4
Wall	5	5						

As can be observed, the results match well with those reported in [34]. Based on Figure 3 and Table 3, responses are evaluated for three different mesh sizes and fluid particle numbers. For the most refined mesh and the most number of particles, differences between FE, FE-SPH, and the reference model in [34] are less than 0.5%. Consequently, the provided numerical models correctly simulate the sloshing phenomenon. Besides, the SPH method is accurate enough to calculate the sloshing height.

4.3 Mesh Sensitivity

Next, some new models with different liquid heights inside the tanks are generated to obtain the optimum element size and fluid particle number. The FEM-SPH approach accuracy depends on the number of structural elements and fluid particles. A set of geometric dimensions for liquid storage tanks is selected. For this geometric configuration, three mesh sizes and three different fluid particle numbers are chosen to achieve a reasonable value. Table 4 illustrates the geometric properties of nine liquid storage tanks considered for mesh sensitivity analysis.

Table 4: Geometric Configuration of tanks for mesh sensitivity analysis

Model	H_l (m)	H_w (m)	2L (m)	t_w (mm)	H_l/2L	Part	Mesh Size		Fluid particles number
							Horizontal	Vertical	
MS1	6	7.5	20	500	0.3	Fluid/Wall	25 25	25 25	1920
MS2	6	7.5	20	500	0.3	Fluid/Wall	10 10	10 10	12000
MS3	6	7.5	20	500	0.3	Fluid/Wall	5 5	5 5	48000
MS4	6	7	20	500	0.3	Fluid/Wall	25 25	25 25	1920
MS5	6	7	20	500	0.3	Fluid/Wall	10 10	10 10	12000
MS6	6	7	20	500	0.3	Fluid/Wall	5 5	5 5	48000
MS7	6	6.5	20	500	0.3	Fluid/Wall	25 25	25 25	1920
MS8	6	6.5	20	500	0.3	Fluid/Wall l	10 10	10 10	12000
MS9	6	6.5	20	500	0.3	Fluid/Wall	5 5	5 5	48000

The object at this subsection is investigating the model accuracy when calculating the maximum sloshing height. Figure 4 and Table 5 show the maximum sloshing height resulted when we have varying sizes of mesh and fluid particle numbers. Three various earthquake records are considered for mesh sensitivity analysis. Each of these earthquake components is applied to only one group of liquid storage tanks with similar geometric characteristics.

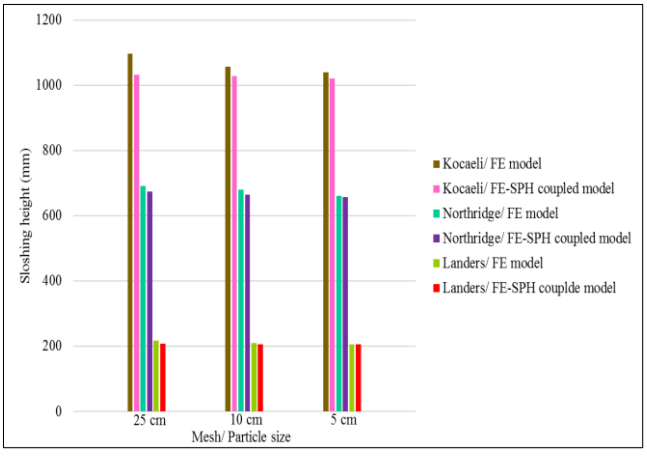

Fig. 4: Mesh sensitivity analysis

Table 5: Mesh sensitivity Analysis

Model	Earthquake (PGA=0.4g)	Part	Mesh size (cm)	Particles number	Maximum sloshing height (mm)		Difference (%)
					FE	FE-SPH	
MS1	Kocaeli	Fluid/wall	25	1920	1097	1032	6.3
MS2		Fluid/wall	10	12000	1056	1028	2.7
MS3		Fluid/wall	5	48000	1039	1021	1.8
MS4	Northridge	Fluid/wall	25	1920	691	673	2.7
MS5		Fluid/wall	10	12000	679	664	2
MS6		Fluid/wall	5	48000	661	657	0.6
MS7	Landers	Fluid/wall	25	1920	217	208	4.3
MS8		Fluid/wall	10	12000	209	206	1.5
MS9		Fluid/wall	5	48000	206	205	0.5

According to the results, in all three seismic loadings, with decreasing element dimensions and increasing the number of particles, the difference between the maximum sloshing height resulted from the finite element model FE and the coupled approach of FE-SPH reduces. By selecting the mesh dimensions equal to 5cm × 5cm having 48000 particles in the liquid, the difference between the results is negligible. Consequently, the element size of 5cm × 5cm is chosen for the finite element modeling. Figure 4 and table 5 show that the selected mesh size and fluid particles are the best in all three seismic loads. So, the chosen dimensions for mesh size and particles are independent of the applied seismic load.

4.4 Sloshing Height in Roofless Tanks

This section concerns on the sloshing height in the roofless tanks considering different tank geometric configurations, liquid heights, and three seismic loads with a scaled PGA of 0.4g. All tanks are shallow. Parameters of the structure and liquid domain are given before. Table 6 shows the modeled tanks geometric properties.

Table 6: Tank configurations for free surface flow investigation

Model	Earthquake	H_l (m)	H_w (m)	2L (m)	H_l/2L	Fluid particles number
SH1		6	7	6	1	14400
SH2	Northridge	9	10	18	0.5	64800
SH3		12	13	48	0.25	230400
SH4		6	7	12	0.5	28800
SH5	El-Centro	9	10	36	0.25	129600
SH6		12	13	12	1	57600
SH7		6	7	24	0.25	57600
SH8	Landers	9	10	9	1	32400
SH9		12	13	24	0.5	115200

Based on Table 6 which is resulted from Taghuchi analysis, the selection of geometric characteristics is such that each H_l value includes all three $\frac{H_l}{2L_x}$ ratios and vice versa. Besides, each earthquake component contains all corresponding values of Hl and ratios of $\frac{H_l}{2L_x}$. Figure 5 shows the time history of sloshing height for different liquid containers, and Table 7 summarizes the extreme values of the sloshing height resulted from FE-SPH coupled models.

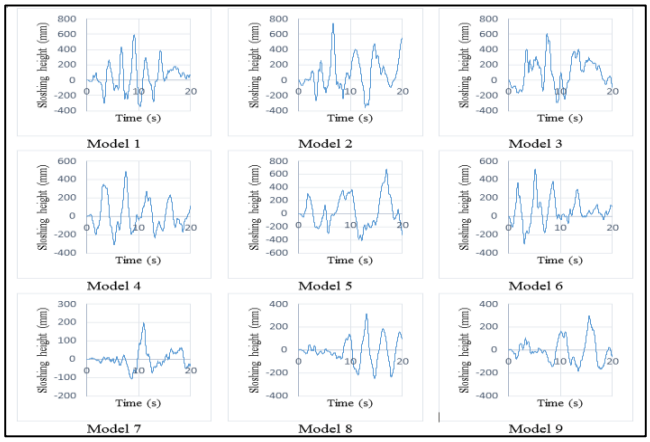

Fig. 5: Time history of sloshing height

Table 7: Extreme values of the sloshing height resulted from FE-SPH coupled models Model Record

Earthquake	Model	d_{max} (mm)	d_{min} (mm)	d_{max}/d_{min}
Northridge	SH1	597	-346	1.73
	SH2	736	-356	2.1
	SH3	608	-293	2.1
El-Centro	SH4	484	-311	1.6
	SH5	675	-417	1.6
	SH6	511	-299	1.7
Landers	SH7	199	-110	1.8
	SH8	314	-248	1.3
	SH9	299	-184	1.6

In Figure 5, the positive values show the upward sloshing, whereas the negative ones represent the downward sloshing. Upward sloshing heights are substantially greater than downward sloshing heights, which are compatible with the results presented by Goudarzi and Sabagh-Yazdi [35]. The difference between the maximum and minimum values of sloshing heights can be due to air and its boundary conditions on the sloshing waves. It seems that air in the upward sloshing movement has less damping property than the liquid in downward sloshing mode. Based on table 6, the maximum and minimum sloshing height of a typical tank change by variation of its geometry parameters, dimensions, and earthquake records' dynamic characteristics.

4.5 Hydrodynamic Pressure in Roofed Tanks

Adequate freeboards for sloshing waves make the design of tanks uneconomical, and some parts of the capacity of tanks under normal loads remain unused. For tanks with an insuficient freeboard, the impact of sloshing waves on the roof inserts undesired hydrodynamic pressures and upward forces on the roof. This section presents the upward hydrodynamic pressure applied on the roof for the liquid containers with tops at point A of the tank (see Figure 1). The freeboard height is zero. The roof and wall of the container are rigid, and their thickness is 500mm. Table 8 shows the roofed tank geometric dimensions and fluid particles number used for the simulation of fluid. Finite element mesh and particle sizes are 5cm × 5cm. Table 8 shows each earthquake component includes all values assigned to H_l and $\frac{H_l}{2L_x}$. Also, each of the values assigned to H_l and $\frac{H_l}{2L_x}$ is common in an analysis. Figure 6 and table 9 show the hydrodynamic pressure time histories and its maximum value acting upward, respectively.

Table 8: Tanks configurations for investigating the upward hydrodynamic pressure on the roof

Earthquake	Model	H_l (m)	H_w (m)	2L (m)	H_l/2L	Fluid particles number
Northridge	HP1	6	6	6	1	14400
	HP2	9	9	18	0.5	64800
	HP3	12	12	48	0.25	230400
El-Centro	HP4	6	6	12	0.5	28800
	HP5	9	9	36	0.25	129600
	HP6	12	12	12	1	57600
Landers	HP7	6	6	24	0.25	57600
	HP8	9	9	9	1	32400
	HP9	12	12	24	0.5	115200

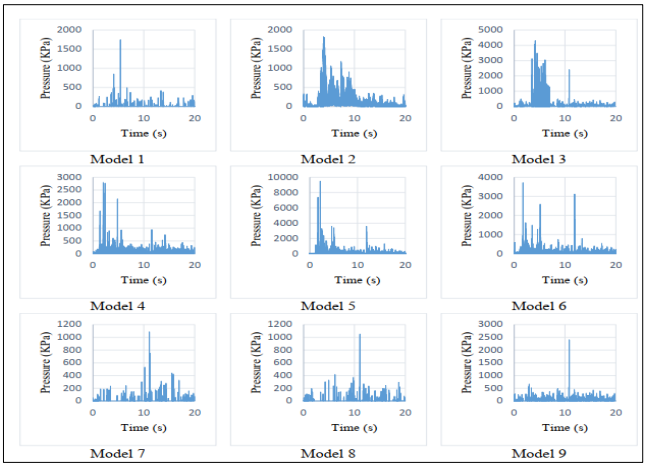

Fig. 6: Time history of the hydrodynamic pressure applied to the roof at Point A (see Figure 1)

Table 9: Tanks configurations for investigating the applied hydrodynamic pressure on the roof

Earthquake	Model	Pressure (Kpa)
Northridge	HP1	1740
	HP2	1820
	HP3	4300
El-Centro	HP4	2800
	HP5	9480
	HP6	3730
Landers	HP7	1080
	HP8	1050
	HP9	2400

The results show that, like roofless tanks, roofed tanks' sloshing phenomenon depends on the tanks' geometric characteristics and the applied earthquake record. The hydrodynamic pressure varies by changing the storage tank dimensions and the applied record as seismic loading. In the following, effects of geometric characteristics and earthquake record properties are investigated in more detail.

4.6 Geometric Properties

This study considers the H_l, $2L_x$, and ratio of $\frac{H_l}{2L_x}$ as the principal geometric parameters that mainly control liquid storage tanks' dynamic responses. The effects of these parameters on the sloshing phenomenon are considered for both roofed and roofless tanks. First, roofless tanks are studied.

Investigating the H_l effects in roofless tanks, model SH7 with model SH9 and model SH4 with model SH6 are compared. Figures 7 and 8 show the sloshing time histories. They have different H_l, but the $2L_x$ is the same, and the freeboard height is 1m (see Table 6). Based on figure 7, the sloshing height of model SH9 is higher than model SH7. Comparison of models SH4 and SH6 demonstrates the same results. Accordingly, if other geometric dimensions are fixed, the liquid height increment will increase the maximum sloshing height as expected.

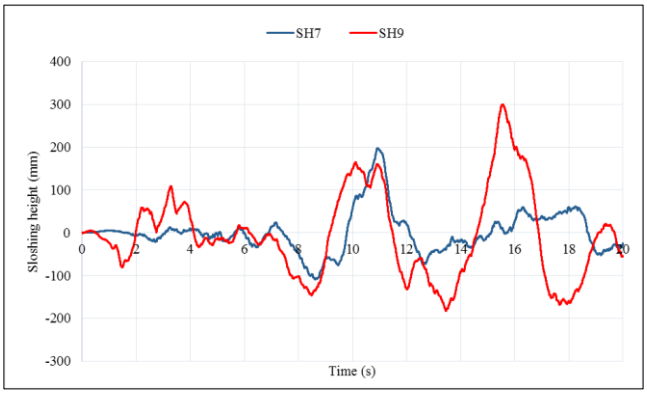

Fig. 7: Comparison between sloshing time histories of models SH7 and SH9; Constant $2L_x$

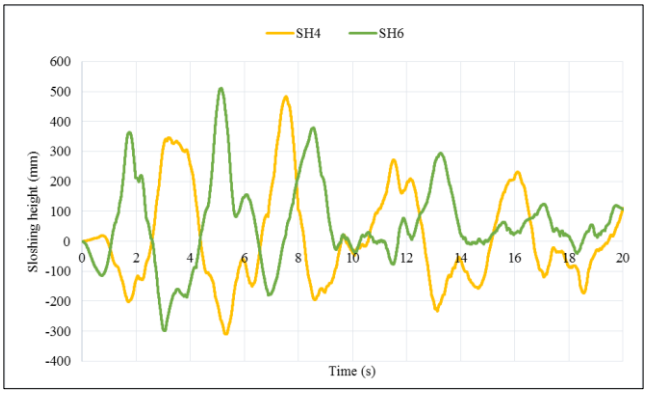

Fig. 8: Comparison between sloshing time histories of models SH4 and SH6; Constant $2L_x$

Next, the effects of liquid height are examined, while other geometric characteristics are variable. This study includes three different H_l, each with a unique $\frac{H_l}{2L_x}$ ratio (regarding the Taguchi analysis result). According to Table 7, in all three seismic loads, tanks with a height of 9m have the maximum sloshing height. Accordingly, the H_l = 9m is the most critical elevation of liquid for the roofless tank. Table 7 shows how significantly the liquid's height which their values are assigned based on the Taguchi method, influences the sloshing height. Besides, it illustrates that the effects of liquid height are more significant than the $\frac{H_l}{2L_x}$ ratio. Figure 5 and table 7 do not show any specific relationship between sloshing height time history and the parameter $\frac{H_l}{2L_x}$. In each of all three seismic loads, the maximum sloshing height occurs at a different ratio of $\frac{H_l}{2L_x}$.

Next, the effects of tank length are investigated, including liquid storage tanks of MS6 and SH1. Models MS6 and SH1 have the same H_l and H_w but different tank lengths $2L_x$. Northridge scaled earthquake is applied to both models of MS6 and SH1. Figure 9 compares the resulted sloshing time

histories. Model MS6 has a maximum sloshing height of 657mm, and model SH1 exhibits a maximum sloshing height equal to 597mm. By approximate tripling the length of the tank, the maximum sloshing height increases only about 10%. It seems that the Taguchi method must consider the parameter $2L_x$ in the category of noise parameters not the main ones in leveling the optimizing problem.

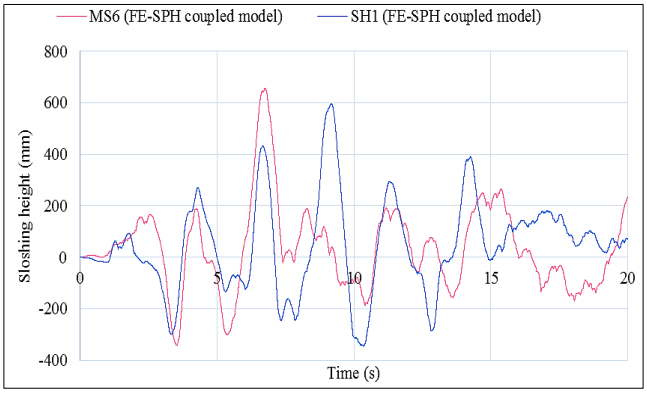

Fig. 9: Comparison between sloshing time histories of models MS6 and SH1; Constant H_l

So, roofless tanks' investigation's geometric properties show that the parameter H_l has more significant effects than both parameters $2L_x$ and $\frac{H_l}{2L_x}$. The presented trends obtained based on the Taguchi method show a considerable deficiency in the expression presented by ACI 350.3-06 [36] known as the code herein. The code employs the idea proposed by Housner and ignores the nonlinear aspect of sloshing phenomenon. For a more accurate comparison, using the code expression, the maximum sloshing height d_{max} is calculated, having the scaled PGA as [36]:

$$d_{max} = LC_cI \tag{13}$$

where I is the importance factor and Cc is the seismic response coeficient which is determined as follows:

$$T_c \le \frac{1.6}{T_s} \rightarrow C_c = \frac{1.5S_{D1}}{T_c} \le 1.5S_{DS} \tag{14}$$

$$T_c > \frac{1.6}{T_s} \rightarrow C_c = \frac{2.4S_{DS}}{T_c^2} \tag{15}$$

$$T_c = \frac{2\pi}{\omega_c} = \left(\frac{2\pi}{\lambda}\right)\sqrt{L} \rightarrow \lambda = \sqrt{3.16gtanh\left[3.16\left(\frac{H_l}{L}\right)\right]} \tag{16}$$

where S_{D1} is the spectral response acceleration, 5% damped, at the period of 1s, Ts is the ratio of design spectral response acceleration at 1s period S_{D1} to that in short periods S_{DS}, T_c is the natural convective period, and S_{DS} is the spectral response acceleration, 5% damped, at a short period. Table 10 shows the maximum sloshing height calculated utilizing the code expressions for the scaled seismic excitation. Figure 10 and Table 11 compare sloshing height resulted from the FE-SPH method with the code.

Table 10: The code maximum sloshing height; Scaled earthquake PGA=0.4g Model

Earthquake	Model	S_{Ds}(g)	S_{D1}(g)	T_s (sec)	1.6/T_s	C_c	d_{max} (mm)
Northridge	SH1	0.884	0.318	0.36	4.44	0.172	517
	SH2	0.884	0.318	0.36	4.44	0.085	765
	SH3	0.884	0.318	0.36	4.44	0.023	549
El-Centro	SH4	1.003	0.401	0.4	4	0.145	868
	SH5	1.003	0.401	0.4	4	0.035	622
	SH6	1.003	0.401	0.4	4	0.154	922
Landers	SH7	0.418	0.147	0.35	4.55	0.022	259
	SH8	0.418	0.147	0.35	4.55	0.065	293
	SH9	0.418	0.147	0.35	4.55	0.030	362

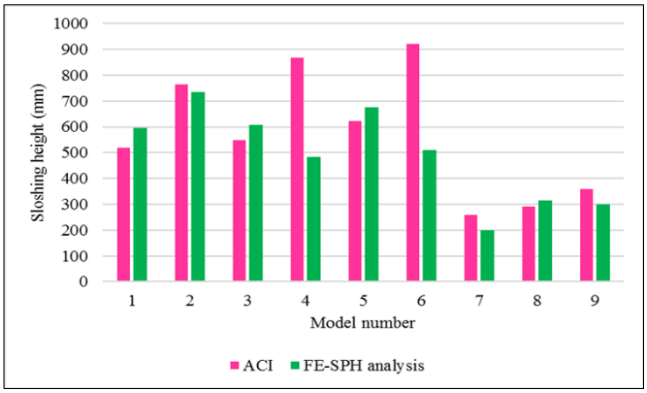

Fig. 10: Comparison between sloshing height calculated by ACI and FE-SPH coupled model

Table 11: Comparison of the code sloshing height with FE-SPH

Earthquake	Model	H_L (m)	H_L/2L	ACI-scaled (mm)	FE-SPH (mm)	difference
Northridge	SH1	6	1	517	597	+15%
	SH2	9	0.5	765	736	-4%
	SH3	12	0.25	549	608	+10%
El-Centro	SH4	6	0.5	868	484	-45%
	SH5	9	0.25	622	675	+8%
	SH6	12	1	922	511	-44%
Landers	SH7	6	0.25	259	199	-23%
	SH8	9	1	293	314	+7%
	SH9	12	0.5	362	299	-17%

As can be seen, there is a significant difference between the calculated maximum sloshing heights. The positive differences show an insuficiency of the code calculated sloshing height. In some liquid storage tanks, the height calculated by the numerical model is greater than the height calculated by the code. At the same time, there are models where the code suggests higher values. Comparison between three heights of 6m, 9m, and 12m shows that differences in absolute values for models with H_l = 9m are less than the other liquid heights under all three seismic loads. Models with H_l = 9m have different ratios of $\frac{H_l}{2L_x}$. So, the proportion of $\frac{H_l}{2L_x}$ is not a decisive parameter. Also, in all seismic loads, the suficiency or insuficiency of the maximum sloshing height calculated by the numerical model compared with the code expressions is the same for models with the liquid height of 6m and 12m. But, they are different from the models that have a liquid height of 9m. For example, under landers earthquake, the maximum sloshing height calculated by the numerical model when H_l = 9m is greater than the one calculated by the code, while for models with the height of 6m and 12m, this value is less than the sloshing height calculated by the code. Such issues again highlight the importance of using the liquid height in the code expressions. Investigating the numerical models' geometric dimensions, the height of the liquid inside the storage tanks Hl has a much more significant effect than the ratio of $\frac{H_l}{2L_x}$. These variations of responses seriously challenge ignoring the liquid height in the relationships presented by the code (Equations 13 to 16).

At this stage, the liquid container dimensions effects on the hydrodynamic pressure applied to the container's roof due to sloshing waves are investigated. The hydrodynamic pressure is calculated assuming zero freeboards. Comparing the model HP4 with HP6 and also, HP7 with HP9 show that in the case with a constant $2L_x$ and under similar seismic loads, as expected, the maximum hydrodynamic pressure on the roof raise by increasing H_l (see Figures 11 and 12). Both models HP4 and HP6, have the liquid length of 12m, and this length in models HP7 and HP9 is 24m. Increasing the liquid height from 6m to 12m (models HP4 and HP6) increases the maximum sloshing height in HP6 by about 30%. For the same increment of H_l but under the Landers earthquake, the maximum sloshing height in the model HP9 is approximately 2.2 times that of model HP7. Although the variation of maximum hydrodynamic pressure is indisputable by an increment of H_l, this increasing range seems to depend on the earthquakes' frequency content because the records are scaled to the PGA = 0.4g. The trend of changes in the maximum sloshing height for roofless tanks also shows the dependency on the frequency content.

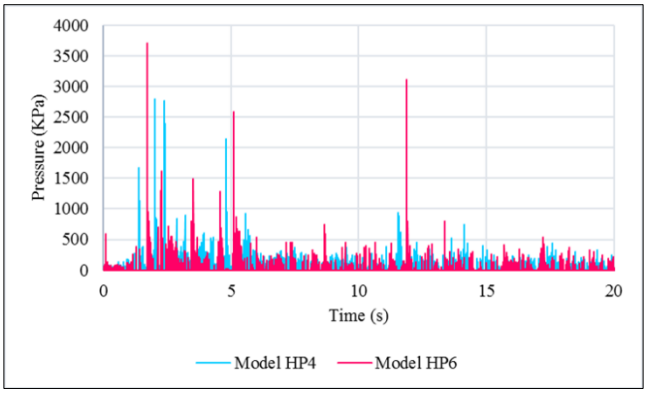

Fig. 11: Hydrodynamic pressure time history; Models HP4 and HP6; El-Centro earthquake

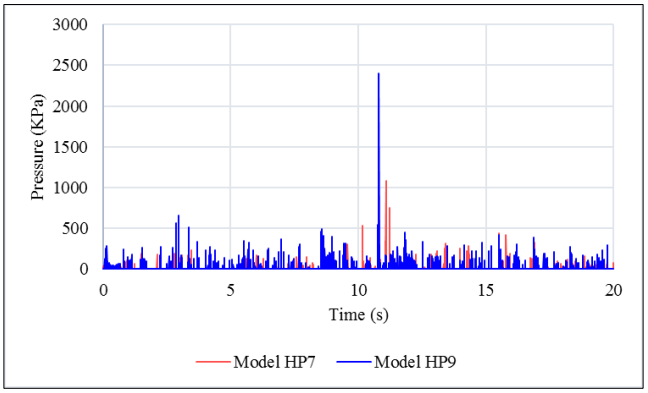

Fig. 12: Hydrodynamic pressure time history; Models HP7 and HP9; El-Centro earthquake

Although increasing the H_l in the liquid storage tanks with the same liquid length increases the maximum hydrodynamic pressure, there is no straightforward relationship between the liquid storage tanks' geometrical characteristics and maximum hydrodynamic pressures. The hydrodynamic pressure takes extreme values in different H_l, $2L_x$, and $\frac{H_l}{2L_x}$ in each earthquake record. Such a sequence is not consistent with the results of roofless tanks.

Comparison of roofless with roofed tanks (see Figures 5 and 7) shows no significant relationship between the sloshing phenomenon in roofed and roofless tanks even having the same geometric characteristics moreover the same exciting records. Such inconsistency is more evident for the maximum sloshing height and maximum hydrodynamic pressure in Tables 7 and 9. For the roofless tanks, all the models having H_l = 9m give a maximum sloshing height. In contrast, for the roofed tanks with zero freeboards, there is no significant relationship between the tank geometrical characteristics and the maximum hydrodynamic pressure. Consequently, if a roofless container with specific geometric dimensions has a maximum sloshing height, it does not mean that the hydrodynamic pressures are maximum for the roofed tank with zero freeboard height and the same geometric dimensions. Even for the roofed and roofless tank

with the same H_l, $2L_x$, and $\frac{H_l}{2L_x}$ the time of occurring the maximum sloshing height and the maximum hydrodynamic pressure are not the same. Table 12 shows the occurrence time of the maximum sloshing height in roofless tanks and that time when occurring the maximum hydrodynamic pressure in roofed tanks. As can be seen, in all liquid storage tanks, the hydrodynamic pressure occurs earlier in roofed tanks in comparison with the moment of happening the maximum sloshing height for open-top tanks.

Table 12: Occurrence time of the maximum sloshing height and the maximum hydrodynamic pressure

Roofless tanks-Sloshing height (mm)			Roofed tanks-Hydrodynamic pressure (Kpa)		
Model	**d_{max} (mm)**	**Time (sec)**	**Model**	**Pressure (Kpa)**	**Time (sec)**
SH1	597	9.18	HP1	1740	5.4
SH2	736	6.67	HP2	1820	3.92
SH3	608	7.43	HP3	4300	4.15
SH4	484	7.54	HP4	2860	2.03
SH5	675	17	HP5	9480	2.21
SH6	511	5.15	HP6	3730	1.73
SH7	199	10.9	HP7	1080	11.1
SH8	314	13.1	HP8	1050	11.1
SH9	299	15.6	HP9	2400	10.8

Accordingly, the roofless tanks' dynamic responses, such as calculated sloshing height, are not a correct parameter for analyzing and determining the applied forces and hydrodynamic pressures on the roof. It is necessary to calculate the dynamic responses of roofed and roofless tanks, separately.

4.7 Earthquake Frequency Content Effects

The calculated sloshing height and hydrodynamic pressure show that the frequency content effects are significant for roofless and roofed tanks. Although all earthquake records have the same PGA = 0.4g, their sloshing height, and hydrodynamic pressure time histories are entirely different. Besides, the amplitudes of responses are significantly different depending on the frequency content. Besides, Table 10 shows that the amplitude of maximum sloshing height calculated by the code is highly dependent on the earthquake frequency properties where we have different sloshing heights despite the equal PGA values for all the considered earthquake records.

The ratio PGA/PGV which is considered as an indicator of the ground motion frequency content, classifies the earthquake records into three categories: 1- high PGA/PGV ratio when PGA/PGV>1.2, 2- moderate PGA/PGV when 0.8< PGA/PGV<1.2, and 3- low PGA/PGV ratio when PGA/PGV<0.8. According to this classification, the Northridge earthquake motion in 1994 with PGA/PGV=0.61 is low frequency-content ground motion, the El-Centro record in 1940 with PGA/PGV=0.88 is categorized as moderate frequency-content, and the Landers record in 1992 has high-frequency content with PGA/PGV=2.41. Table 13 compares the highest maximum sloshing height and the highest maximum hydrodynamic pressures of three earthquake records with their corresponding PGA/PGV ratio.

Table 13: Maximum sloshing height and hydrodynamic pressure in three input frequency contents

Earthquake	PGA/PGV ratio		Roofless tank		Roofed tank	
			Model	**Maximum d_{max} (mm)**	**Model**	**Maximum P_{max} (Kpa)**
Northridge	0.61	Low	SH2	736	HP3	4300
El-Centro	0.88	Moderate	SH5	675	HP5	9480
Landers	2.41	High	SH8	314	HP9	2400

According to Table 13, for both roofed and roofless liquid storage tanks, a high-frequency content Landers record causes lower sloshing waves than the other two records. But, in a tank without a roof, the Northridge earthquake record having low-frequency content causes a maximum sloshing height. In contrast, for the roofed tanks, the El-Centro earthquake with a moderate frequency content causes a higher maximum hydrodynamic pressure. So, the effects of earthquake frequency content on roofed and roofless storage tanks are different. It is essential to consider the liquid/structure dynamic properties effects on the sloshing phenomenon to evaluate the frequency content effects more accurately. The ratio of PGA/PGV indicates only the frequency content of earthquakes.

Next, the natural vibrating frequencies of the contained liquid are determined by modal analysis and considered with the response spectra of the earthquake records simultaneously to study both the dynamic properties of liquid storage tanks and the seismic excitation frequency contents. Responses are compared with the natural frequencies obtained by the code expressions. The code calculates the natural periods of impulsive and convective parts separately (See Tables 14 and 15).

Table 14: Natural vibrating periods/frequencies for the convective component of the liquid contained

	Convective					
	ACI			FEM-SPH		
Model	T_c (sec)	f_c (Hz)	W_c/W_L	T_c (sec)	f_c (Hz)	W_c/W_L
SH1	2.769	0.361	0.263	2.8	0.357	0.053
SH2	4.995	0.2	0.485	5.055	0.198	0.285
SH3	9.635	0.104	0.695	9.725	0.103	0.485
SH4	4.079	0.245	0.485	4.109	0.243	0.285
SH5	8.344	0.12	0.695	8.404	0.119	0.485
SH6	3.916	0.255	0.263	3.946	0.253	0.053
SH7	6.813	0.147	0.695	6.873	0.145	0.485
SH8	3.392	0.295	0.263	3.422	0.292	0.053
SH9	5.768	0.173	0.485	5.828	0.172	0.285

Table 15: Natural vibrating periods/frequencies for the impulsive component of the liquid contained

	Impulsive					
	ACI			FEM-SPH		
Model	T_i (sec)	f_i (Hz)	W_i/W_L	T_i (sec)	f_i (Hz)	W_i/W_L
SH1	0.026	37.748	0.808	0.032	31.509	0.692
SH2	0.063	15.988	0.542	0.059	16.837	0.464
SH3	0.122	8.186	0.288	0.124	8.042	0.247
SH4	0.026	38.205	0.542	0.035	28.289	0.464
SH5	0.064	15.172	0.288	0.087	11.434	0.247
SH6	0.119	8.392	0.808	0.08	12.463	0.692
SH7	0.027	37.736	0.288	0.053	18.866	0.247
SH8	0.063	15.960	0.808	0.056	17.808	0.692
SH9	0.120	8.354	0.542	0.085	11.786	0.464

In this table, T_c is the natural vibrating period of the convective term in the contained liquid, T_i is that for the impulsive part, f_c and f_i are the corresponding frequencies, respectively. A comparison of FEM-SPH and ACI 350.3-06 results shows that the FE-SPH results are in good agreement with the analytical values for the convective and impulsive parts. The impulsive part which is near the tank's base only contributes to the base shear and overturning moment. The convective part is in the upper part of the tank, which mainly controls the sloshing phenomenon, which is the study's main subject. Accordingly, in the current practice, the natural vibrating period of the convective component in the contained liquid and the earthquake response spectra are considered simultaneously to investigate the frequency content's effects on the sloshing phenomenon (see Figures 13, 14, and 15).

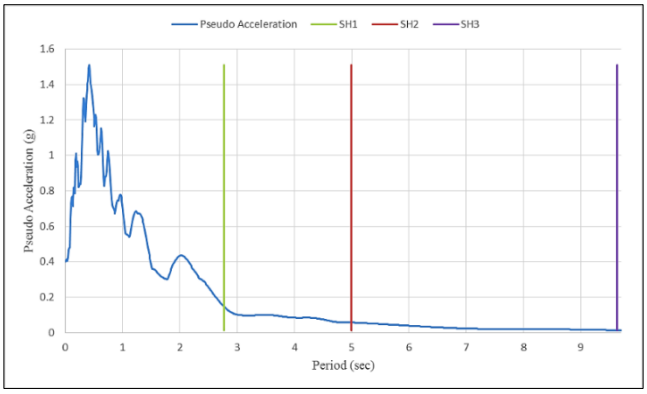

Fig. 13: Response spectrum of the Northridge scaled earthquake and convective periods of models SH1, SH2, and SH3

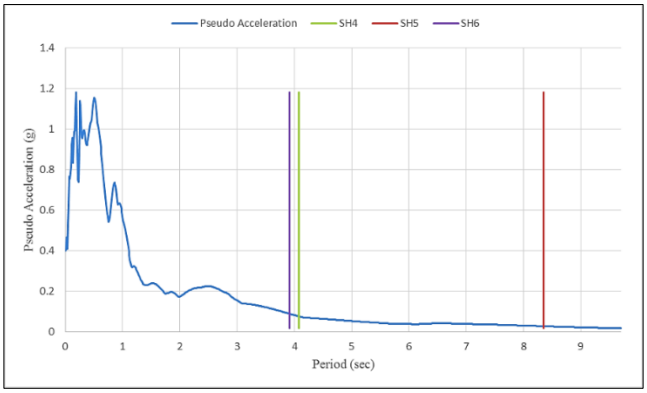

Fig. 14: Response spectrum of the El-Centro scaled earthquake and convective periods of models SH4, SH5, and SH6

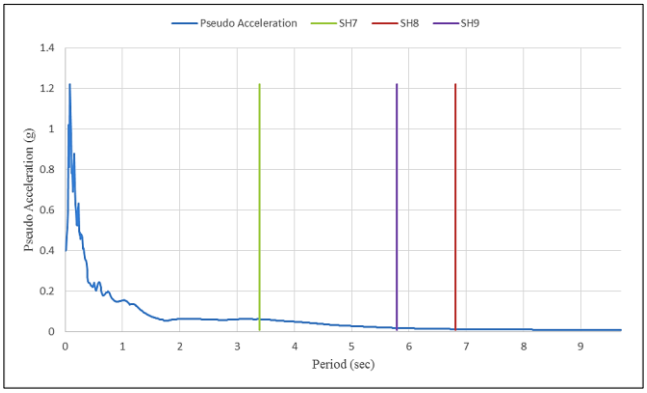

Fig. 15: Response spectrum of the Landers scaled earthquake and convective periods of models SH7, SH8, and SH9

Figures 13 to 15 show that the pseudo acceleration PSA values corresponding to the T_c are negligible. Consequently, T_c and the response spectra of the records are not indicating parameters that correctly exhibits the frequency content effects on the sloshing waves. Figures 16 to 18 show an interval of 0s to 0.5s from the relevant response spectra including the lines indicating T_i values of the contained liquid having various dimensions.

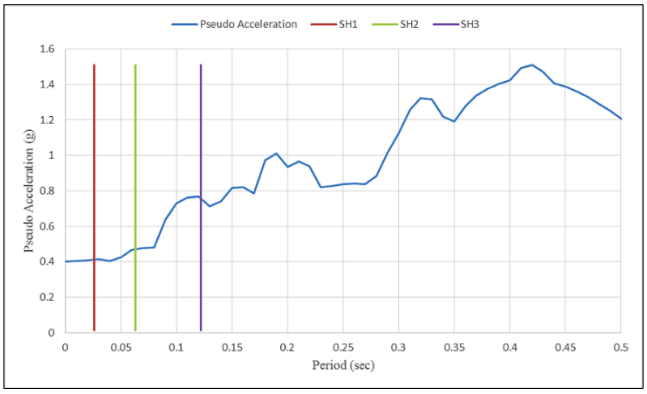

Fig. 16: Response spectrum of the Northridge scaled earthquake and impulsive periods of models SH1, SH2, and SH3

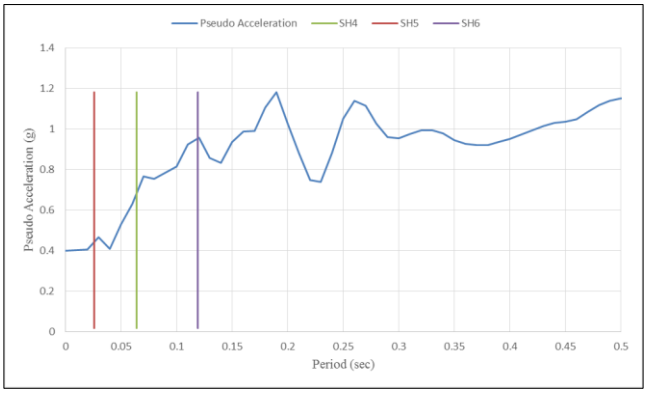

Fig. 17: Response spectrum of the El-Centro scaled earthquake and impulsive periods of models SH4, SH5, and SH6

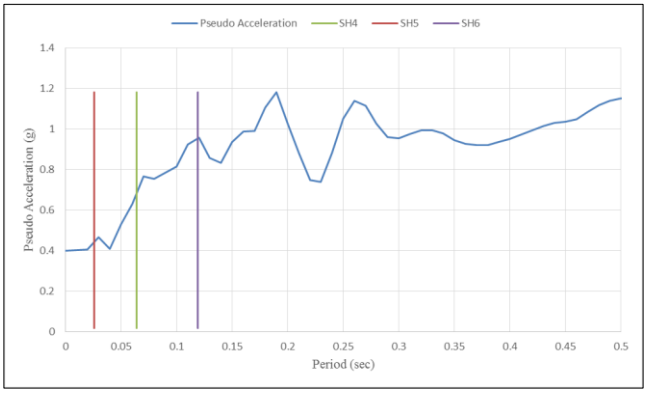

Fig. 18: Response spectrum of the Landers scaled earthquake and impulsive periods of models SH7, SH8, and SH9

Figures 16 to 18 show that PSA values corresponding to T_i are more consistent with the sloshing wave height. The PSA values are significant within the natural impulsive period T_i range. But, its value is close to zero within the range of natural convective period T_c. Although the PSA values in the range of T_i values are more consistent with the dynamic responses caused by the sloshing phenomenon, the sloshing height trend is still not compatible with the PSA. In the Northridge earthquake record, the SH2 model has the maximum sloshing height. According to Figure 16, PSA at T_i corresponding to the model SH3 is higher than the PSA corresponding to the SH2 model. In the Landers earthquake, PSA corresponding to the SH7 is less than that relevant to the SH9 model, and the maximum sloshing height for SH9 model is nearly 50% higher than the sloshing height resulted for the model SH7. So, although the calculated T_i values are more consistent with the calculated response spectra and sloshing height curves in comparison with the values of T_c, there is still no proper correspondence between the contained liquid T_i and the sloshing height variation.

The code assumes that the tank wall is rigid, and appropriate modifications are made in the expressions to apply this assumption. Accordingly, it is better to consider another parameter to investigate the effect of earthquake frequency content. The results show that the earthquake frequency content and the contained liquid vibration characteristics, including the natural vibration period, affect the sloshing phenomenon. Therefore, using a parameter that includes these two components concurrently can be a better indicator of the sloshing phenomenon.

Based on the natural vibrating properties of the contained liquid in the tanks, the acceleration spectrum intensity may be a good indicator that was initially recommended for seismic analysis of concrete dams. Bradley mentioned that the acceleration spectrum intensity ASI is a good intensity measure for short period structures [37]. Thun et al. introduced the acceleration spectrum intensity ASI as the integral of the pseudo-spectral acceleration for a range of periods from 0.1s to 0.5s [38]. The expression for ASI is given as [38]:

$$ASI = \int_{0.1}^{0.5} Sa(T, 5\%)dT \quad (17)$$

where Sa(T,5%) is the 5% damped spectral acceleration at a specific vibration period T.

Table 16 compares each earthquake record's ASI with their corresponding highest maximum sloshing height and highest maximum hydrodynamic pressure resulted from the analyses.

Table 16: Acceleration spectrum intensity for roofless liquid storage tanks-maximum sloshing height

Earthquake	ASI (g×sec)	Roofless tank		Roofed Tank	
		Model	Maximum d_{max} (mm)	Model	Maximum P_{max} (Kpa)
Northridge	0.442	SH2	736	HP3	4300
El-Centro	0.394	SH4	675	HP5	9480
Landers	0.185	SH6	314	HP9	2400

Table 16 shows that the maximum sloshing height is higher for an earthquake with a maximum ASI, and an earthquake with a lower ASI gives a lower maximum sloshing height. However, the earthquake with the maximum ASI does not

have the highest maximum hydrodynamic pressure and vice versa. A more detailed investigation on table 16 shows that the maximum sloshing height ratio in the two earthquakes is proportional to their ASI values ratio. Table 17 presents these ratios. The differences between the ASI ratio and the maximum sloshing height ratio corresponding to the two earthquake records are less than 3%.

Table 17: the ratio of ASIs and its correspondence with the ratio of d_{max}

Model	Ratio of maximum d_{max}	Earthquake	Ratio of ASI (g×sec)	Differences
SH2/SH5	1.09	Northridge/ El-Centro	1.12	2.8%
SH2/SH8	2.34	Northridge / Landers	2.39	2.1%
SH5/SH8	2.15	El-Centro /Landers	2.13	0.9%

Table 18 compares the ASI ratio for the three earthquake records with the proportion of maximum hydrodynamic pressure under the same records for the roofed tanks. The results indicates that the maximum hydrodynamic pressure ratio is not related to the corresponding ASI ratio. The collision of sloshing waves with the roof may cause discrepancies between the ASI and maximum hydrodynamic pressure ratios. The sloshing waves' impact on the roof changes their oscillation characteristics and vibration properties.

Table 18: the ratio of ASIs and its correspondence with the ratio of Pressures (kPa)

Model	Ratio of maximum P_{max}	Earthquake	Ratio of ASI (g×sec)	Differences
HP3/HP5	0.45	Northridge/ El-Centro	1.12	148.8%
HP3/HP9	1.79	Northridge / Landers	2.39	41.8%
HP5/HP9	3.95	El-Centro /Landers	2.13	46.1%

4.8 The signal-to-noise ratio in Taguchi design

In the current work, a statistical analysis of the sloshing phenomenon and the investigation of applied pressure to the roof in 2D rectangular tanks was conducted using Taguchi technique under numerical analysis with the regression equation.

From the results, "the smaller is the better" condition examines the optimum controlling parameters. The Taguchi method presents the initial optimized values for the liquid height and its length. Table 19 shows design parameter values and their associated levels.

Table 19: Design parameters values and their corresponding levels in Taghuchi method Level

Design parameters	Type	Value	Level
Seismic loading-Northridge	PGA/PGV (1/sec)	<0.8	1
Seismic loading-El-Centro	PGA/PGV (1/sec)	<0.8 and <1.2	2
Seismic loading-Landers	PGA/PGV (1/sec)	>1.2	3
Geometric configuration	H_L (m)	6	1
Geometric configuration	H_L (m)	9	2
Geometric configuration	H_L (m)	12	3
Dimensionless Geometric configuration	H_l/L	1	1
Dimensionless Geometric configuration	H_l/L	0.5	2
Dimensionless Geometric configuration	H_l/L	0.25	3

Table 20 shows the corresponding maximum sloshing height and maximum applied Pressures to the tank's roof for all levels of considered design parameters.

Table 20: Summary of the sloshing height and applied pressures on the roof

Earthquake	PGA/PGV	H_l (m)	H_l/L	d_{max} (mm)	Pressure (kPa)
Northridge	0.57	6	1	597	348
		9	0.5	736	365
		12	0.25	608	860
El-Centro	0.88	6	0.5	484	559
		9	0.25	675	1900
		12	1	511	742
Landers	2.44	6	0.25	199	217
		9	1	314	210
		12	0.5	299	480

Figure 19 shows the signal-to-noise ratio of maximum sloshing height calculated based on "the smaller is the better" for the roofless tanks.

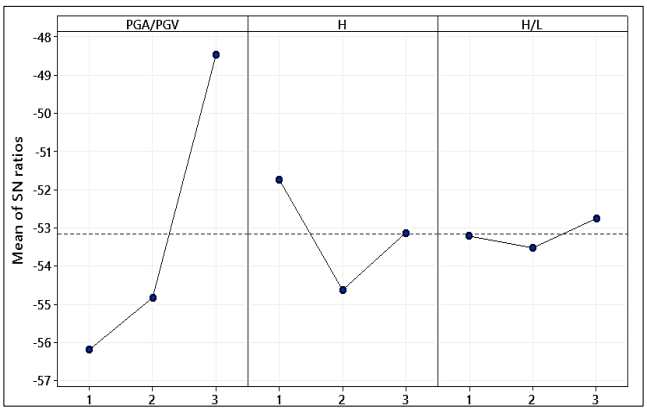

Fig. 19: Statistical results for the sloshing height in roofless tanks

The following results can be obtained from Figure 19:

- Increasing the level of PGA/PGV (moving from low frequency to high-frequency contents) decreases the sloshing height in all the containers.
- The effect H_l is not low. However, there is no straight relationship between the sloshing height and H_l in the considered range of geometric dimensions.
- The effect $\frac{H_l}{2L_x}$ on the sloshing height is low.

Figure 20 shows the signal-to-noise ratio for the upward hydrodynamic pressure applied to the roof in the roofed tanks. Considering this figure, the following results are observed:

- When the level of PGA/PGV increases (which means moving from low-frequency earthquake to high frequency): The upward pressure applied on the roof increases as moving from the low to moderate frequency earthquake; This pressure decreases as moving from the moderate to high-frequency content.
- When the H_l level increases (meaning that the liquid height increases), the upward pressure applied on the roof increases.
- When the level of $\frac{H_l}{2L_x}$ increases (decreasing the ratio from 1 to 0.25 means increasing the container's length), the applied up warding pressure increases.

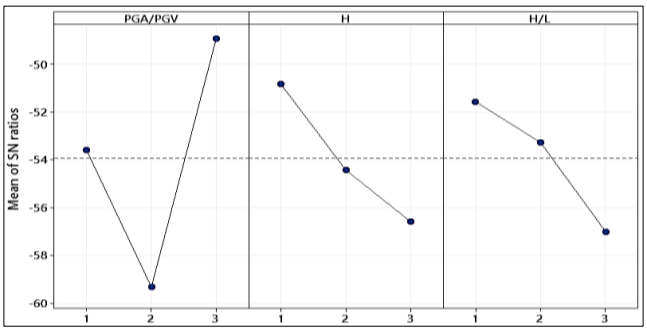

Fig. 20: Statistical results for the maximum hydrodynamic pressure in the roofless tanks

5. Concluding Remarks

This study concerns the sloshing phenomenon in roofed and roofless liquid storage tanks employing the coupled FE-SPH approach considering the effects of the liquid storage tanks' geometric dimensions and scaled earthquake records frequency contents. The liquid height Hl, its length $2L_x$, and the ratio of these two parameters $\frac{H_l}{2L_x}$ are geometric parameters. Three scaled horizontal earthquake records of Northridge 1994, El-Centro 1940, and Landers 1992, which are scaled at PGA = 0.4g, are applied to the liquid storage tanks as the low, moderate and high frequency content records, respectively. Based on the introduced concept by Taguchi, a series of analyses are designed so that we have the effect of predefined parameters in the responses utilizing the optimization procedures employed by the Taguchi method.

Results show that the sloshing phenomenon in both roofed and roofless tanks depends on geometric dimensions. The hydrodynamic pressure concerning roofed tanks exhibits increasing when Hl increases. For roofless tanks, the time history of the sloshing height shows that the liquid height H_l is more important than $2L_x$ and $\frac{H_l}{2L_x}$. Regardless of other geometric characteristics and seismic loading, the roofless tank's sloshing height is maximum for a liquid height of 9m in the considered set of analyses. But, the parameter $\frac{H_l}{2L_x}$ does not have any specific contribution to the sloshing height of roofless tanks.

Comparison of maximum sloshing height calculated by ACI 350.3-06 and FE-SPH coupled model in this study challenges the code expressions for the sloshing phenomenon. Based on code equations, the ratio of $\frac{H_l}{2L_x}$ and $2L_x$ are geometric parameters of the tank that participates in calculating the maximum sloshing height. And, the proportion of $\frac{H_l}{2L_x}$ only contributes to calculations of Tc. This study shows that the liquid's height is the most important geometric property. So, the expressions of ACI 350.3-06 need some revision to consider the liquid height H_l.

Time histories of Sloshing height and hydrodynamic pressure exhibit that the earthquake frequency content is a more influential factor than geometric configuration. One should consider the frequency content of earthquake records and the contained liquid's dynamic characteristics simultaneously to investigate the effects of frequency content on the sloshing phenomenon. Considering the ratio of PGA to PGV as a frequency content indicator, the effects of frequency contents are different for roofed and roofless tanks. This criterion includes only the frequency content of the earthquake record independent of the contained liquid natural vibrating period. So, a more comprehensive criterion is needed.

Response spectra of earthquake records with T_c and T_i, as another criterion, do not correctly show the earthquake frequency content effects on the sloshing phenomenon due to the assumptions made for their calculations. The Pseudo acceleration is limited in values corresponding to Tc. Also, the acceleration values according to T_i are more consistent with the height of the sloshing waves. However, the Pseudo-acceleration variations are not consistent with the maximum sloshing height variations in terms of T_i.

Acceleration spectrum intensity ASI is considered as another criterion. Comparisons of the sloshing height for different earthquake records show that the ASI can be a good criterion for expressing frequency content effects on the roofless tanks' sloshing phenomenon. The ASI can predict

the relationship between the earthquake frequency content and the sloshing phenomenon in roofless tanks, but this relationship has more complexity in roofed tanks. Still, in roofed tanks, frequency content effects are associated with more complexity.

The Taguchi analysis, including "the smaller is the better" as a signal to noise ratio verifies the dependency of the sloshing phenomenon on the geometric dimensions and the frequency content of the earthquake record. The results of the current study must be used for further Taguchi analyses. For the following Taguchi analysis, due to the importance and consequence of the frequency content on the sloshing phenomenon, it is essential to consider the frequency content of earthquake records as a design parameter. This study shows that ASI is the best design parameter that indicates the frequency content effects on the sloshing phenomenon. But, it is recommended to choose PGA of records as a noise parameter. It is also suggested to select the Hl as the design parameter, but the $2L_x$ and $\frac{H_l}{2L_x}$ should be considered as the noise parameter.

References

[1] Westergaard, H. M. (1933). Water pressures on dams during earthquakes. Transactions of the American society of Civil Engineers, 98(2), 418-433.

[2] Jacobsen, L. S. (1949). Impulsive hydrodynamics of fluid inside a cylindrical tank and of fluid surrounding a cylindrical pier. Bulletin of the Seismological Society of America, 39(3), 189-204.

[3] Housner, G. W. (1957). Dynamic pressures on accelerated fluid containers. Bulletin of the seismological society of America, 47(1), 15-35.

[4] Housner, G. W. (1963). The dynamic behavior of water tanks. Bulletin of the seismological society of America, 53(2), 381-387.

[5] Mostafaei, H., Behnamfar, F., & Alembagheri, M. (2022). Reliability and sensitivity analysis of wedge stability in the abutments of an arch dam using artificial neural network. Earthquake Engineering and Engineering Vibration, 21(4), 1019-1033.

[6] Mostafaei, H., Mostofinejad, D., Ghamami, M., & Wu, C. (2023). A new approach of ensemble learning in fully automated identification of structural modal parameters of concrete gravity dams: A case study of the Koyna dam. Structures, 50, 255-271.

[7] Mashayekhi, M., & Mostafaei, H. (2020). Determining the critical intensity for crack initiation in concrete arch dams by endurance time method. Numerical Methods in Civil Engineering, 5(2), 21-32.

[8] Haroun, M. A., & Tayel, M. A. (1985). Response of tanks to vertical seismic excitations. Earthquake engineering & structural dynamics, 13(5), 583-595.

[9] Babu, S. S., & Bhattacharyya, S. K. (1996). Finite element analysis of fluid-structure interaction effect on liquid retaining structures due to sloshing. Computers & structures, 59(6), 1165-1171.

[10] Virella, J. C., Prato, C. A., & Godoy, L. A. (2008). Linear and nonlinear 2D finite element analysis of sloshing modes and pressures in rectangular tanks subject to horizontal harmonic motions. Journal of Sound and Vibration, 312(3), 442-460.

[11] Kianoush, M. R., & Ghaemmaghami, A. R. (2011). The effect of earthquake frequency content on the seismic behavior of concrete rectangular liquid tanks using the finite element method incorporating soil–structure interaction. Engineering structures, 33(7), 2186-2200.

[12] Manser, W. S., Touati, M., & Barros, R. C. (2017). The maximum sloshing wave height evaluation in cylindrical metallic tanks by numerical means. In MATEC Web of Conferences95, 17005.

[13] Zhang, Y., & Wan, D. (2018). MPS-FEM coupled method for sloshing flows in an elastic tank. Ocean Engineering, 152, 416-427.

[14] Liu, G. R., & Liu, M. B. (2003). Smoothed particle hydrodynamics: a meshfree particle method. World scientific.

[15] Gingold, R. A., & Monaghan, J. J. (1977). Smoothed particle hydrodynamics: theory and application to non-spherical stars. Monthly notices of the royal astronomical society, 181(3), 375-389.

[16] Lucy, L. B. (1977). A numerical approach to the testing of the fission hypothesis. Astronomical Journal, 82, 1013-1024.

[17] Groenenboom, P. H., & Cartwright, B. K. (2010). Hydrodynamics and fluid-structure interaction by coupled SPH-FE method. Journal of Hydraulic Research, 48(sup1), 61-73.

[18] Hu, D., Long, T., Xiao, Y., Han, X., & Gu, Y. (2014). Fluid–structure interaction analysis by coupled FE–SPH model based on a novel searching algorithm. Computer Methods in Applied Mechanics and Engineering, 276, 266-286.

[19] Nunez-Ramirez, J., Marongiu, J. C., Brun, M., & Combescure, A. (2017). A partitioned approach for the coupling of SPH and FE methods for transient nonlinear FSI problems with incompatible time-steps. International Journal for Numerical Methods in Engineering, 109(10), 1391-1417.

[20] Han, L., & Hu, X. (2018). SPH modeling of fluid-structure interaction. Journal of Hydrodynamics, 30, 62-69.

[21] D Jena and K C Biswal. Violent sloshing and wave impact in a seismically excited liquid-filled tank: Meshfree particle approach. Journal of Engineering Mechanics, 144(3), 04017182. doi: 10.1061/(ASCE) EM.1943-7889.0001364.

[22] Xu, Y., Yu, C., Liu, F., & Liu, Q. (2019). A coupled NMM-SPH method for fluid-structure interaction problems. Applied Mathematical Modelling, 76, 466-478.

[23] Dinçer, A. E., Demir, A., Bozkuş, Z., & Tijsseling, A. S. (2019). Fully Coupled Smoothed Particle Hydrodynamics-Finite Element Method Approach for Fluid–Structure Interaction Problems With Large Deflections. Journal of Fluids Engineering, 141(8), 081402.

[24] Moslemi, M., Farzin, A., & Kianoush, M. R. (2019). Nonlinear sloshing response of liquid-filled rectangular concrete tanks under seismic excitation. Engineering Structures, 188, 564-577.

[25] Ng, K. C., Alexiadis, A., Chen, H., & Sheu, T. W. H. (2020). A coupled smoothed particle hydrodynamics-volume compensated particle method (SPH-VCPM) for fluid structure interaction (FSI) modelling. Ocean Engineering, 218, 107923.

[26] Kalateh, F., & Koosheh, A. (2020). Simulation of cavitating fluid–Structure interaction using SPH–FE method. Mathematics and Computers in Simulation, 173, 51-70.

[27] Varas, D., Zaera, R., & López-Puente, J. (2009). Numerical modelling of the hydrodynamic ram phenomenon. International Journal of Impact Engineering, 36(3), 363-374.

[28] Kackar, R. N. (1985). Off-line quality control, parameter design, and the Taguchi method. journal of Quality Technology, 17(4), 176-188.

[29] Leon, R. V., Shoemaker, A. C., & Kacker, R. N. (1987). Performance measures independent of adjustment: an explanation and extension of Taguchi's signal-to-noise ratios. Technometrics, 29(3), 253-265.

[30] Pignatiello Jr, J. J. (1988). An overview of the strategy and tactics of Taguchi. IIE transactions, 20(3), 247-254.

[31] Tsui, K. L. (1992). An overview of Taguchi method and newly developed statistical methods for robust design. Iie Transactions, 24(5), 44-57.

[32] Ground motion database. https://peer.berkeley.edu/peer-strong-ground-motion-databases.

[33] Elnashai, A. S., & Di Sarno, L. (2015). Fundamentals of earthquake engineering: from source to fragility. John Wiley & Sons.

[34] Kianoush, M. R., Mirzabozorg, H., & Ghaemian, M. (2006). Dynamic analysis of rectangular liquid containers in three-dimensional space. Canadian Journal of Civil Engineering, 33(5), 501-507.

[35] Goudarzi, M. A., & Sabbagh-Yazdi, S. R. (2012). Investigation of nonlinear sloshing effects in seismically excited tanks. Soil Dynamics and Earthquake Engineering, 43, 355-365.

[36] ACI Committee 350.3-06. (2006). Seismic design of liquid-containing concrete structures (ACI 350.3-06) and commentary (ACI 350.3R-06). American Concrete Institute (ACI), Farmington Hills, United States.

[37] Bradley, B. A. (2010). Site-specific and spatially distributed ground-motion prediction of acceleration spectrum intensity. Bulletin of the Seismological Society of America, 100(2), 792-801.

[38] Thun, J., Roehm, L. H., Scott, G. A., & Wilson, J. (1988). Earthquake ground motions for design and analysis of dams. Geotechnical special publication, 20, 463– 481.